

# Nanoscale

Accepted Manuscript



This is an *Accepted Manuscript*, which has been through the Royal Society of Chemistry peer review process and has been accepted for publication.

*Accepted Manuscripts* are published online shortly after acceptance, before technical editing, formatting and proof reading. Using this free service, authors can make their results available to the community, in citable form, before we publish the edited article. We will replace this *Accepted Manuscript* with the edited and formatted *Advance Article* as soon as it is available.

You can find more information about *Accepted Manuscripts* in the [Information for Authors](#).

Please note that technical editing may introduce minor changes to the text and/or graphics, which may alter content. The journal's standard [Terms & Conditions](#) and the [Ethical guidelines](#) still apply. In no event shall the Royal Society of Chemistry be held responsible for any errors or omissions in this *Accepted Manuscript* or any consequences arising from the use of any information it contains.

# Deep-Ultraviolet-Light-Driven Reversible Doping of WS<sub>2</sub> Field-Effect Transistor

Muhammad Waqas Iqbal<sup>1</sup>, Muhammad Zahir Iqbal<sup>1</sup>, Muhammad Farooq Khan<sup>1</sup>, Muhammad Arslan Shehzad<sup>2</sup>, Yongho Seo<sup>2</sup>, Jonghwa Eom<sup>1\*</sup>

<sup>1</sup>Department of Physics and Graphene Research Institute, Sejong University, Seoul 143-747, Korea.

<sup>2</sup>Faculty of Nanotechnology & Advanced Materials Engineering and Graphene Research Institute, Sejong University, Seoul 143-747, Korea.

E-mail: eom@sejong.ac.kr

**ABSTRACT:** Improvement of the electrical and photoelectric characteristics is essential to get advanced performance of field effect transistors and optoelectronic devices. Here we have developed a doping technique to drastically improve electrical and photoelectric characteristics of single-layer, bi-layer and multi-layer WS<sub>2</sub> field effect transistor (FET). After illuminated by deep ultraviolet (DUV) light under nitrogen environment, WS<sub>2</sub> FET shows enhanced charge carrier density, mobility and photocurrent response. Threshold voltage of WS<sub>2</sub> FET shifted toward negative gate voltage, and the positions of E<sub>2g</sub><sup>1</sup> and A<sub>1g</sub> peaks in Raman spectra shifted toward lower wave numbers, indicating the n-type doping effect of the WS<sub>2</sub> FET. The doping effect is reversible. The pristine characteristics of WS<sub>2</sub> FET can be restored by DUV light illumination under oxygen environment. The DUV-driven doping technique under gas environment provides a very stable, effective, easily-applicable way to enhance the performance of WS<sub>2</sub> FET.

**KEYWORDS:** tungsten disulfide (WS<sub>2</sub>), deep-ultraviolet light, field-effect transistor, doping, photocurrent

## 1. Introduction

Two-dimensional (2D) layered materials draw significant interest because of their unique physical and electrical properties. For example, graphene is an important material for atomic-layer electronic device applications because of its numerous advantages,<sup>1</sup> such as exceptionally high carrier mobility at room temperature,<sup>2</sup> mechanical strength,<sup>3,4</sup> flexibility,<sup>5</sup> and various doping effects<sup>6</sup> that lead to technological applications in nanoelectronics, optoelectronics, energy harvesting, and sensors.<sup>7-9</sup> However, graphene is not a promising material for active channels in field-effect transistors (FETs) because of the absence of a bandgap in the pristine state.<sup>10,11</sup> Numerous trials are conducted to generate a bandgap in graphene by patterning to nanostructures,<sup>12,13</sup> chemical functionalization,<sup>14</sup> and dual-gated bilayer graphene.<sup>15,16</sup> However, only a narrow bandgap is achieved and the low on/off switching ratio is too small to be applicable to FETs.

Owing to considerable bandgaps of around 1–2 eV,<sup>17-19</sup> 2D transition-metal dichalcogenides (TMDCs) draw a great deal of research attention for FET and optoelectronic device applications.<sup>20,21</sup> In particular, tungsten- and molybdenum-based TMDC compounds are attracting great interest due to semiconducting properties and bandgaps that extend from visible to near-infrared regime.<sup>22,23</sup> An interesting property of tungsten disulfide ( $\text{WS}_2$ ) is that it transitions to a direct bandgap material when cleaved into a monolayer.<sup>20</sup> Bulk  $\text{WS}_2$  is an indirect bandgap (1.4 eV) semiconductor but turns into a direct bandgap (2.1 eV) material when exfoliated into the monolayer.<sup>24</sup> A single layer of  $\text{WS}_2$  crystal is formed by covalently bonded in-plane S-W-S atoms, which consist of two sheets of S and one sheet of W atoms and are hexagonally packed.<sup>24-26</sup> As adjacent layers in  $\text{WS}_2$  crystals are bound together by weak van der Waals forces, mono- or few-layer  $\text{WS}_2$  can be fabricated through micromechanical cleavage.  $\text{WS}_2$  also offers distinct advantages over other 2D materials because it is chemically stable and only has a weak impurity band.<sup>18,27,28</sup> It has very high on/off output current ratio in FET devices, high thermal stability, no dangling bonds, and electrostatic integrity.<sup>29</sup> High

mobility comparable to that of silicon makes  $\text{WS}_2$  a new competitor to graphene and traditional semiconductors in a variety of applications, such as low-power FETs, optoelectronic devices, memory devices, and chemical sensors.

However, degradation in transport properties is often observed in 2D materials such as  $\text{MoS}_2$ - and  $\text{WS}_2$ -based devices, most likely due to extrinsic or environmental effects.<sup>22,30,31</sup> These effects or defects limit the intrinsic properties and overall performance of a device. Therefore, studying the possible factors that influence the reliability of atomically thin 2D material devices is of technological and scientific importance.<sup>20,24</sup> Researchers attempt to improve the performance of 2D materials by using different metal contacts (source and drain electrodes), scaling down device dimensions, using high-K materials for gate dielectric, and doping with self-assembled monolayers or molecules with metal nanoparticles.<sup>32–34</sup> Similar to other low-dimensional semiconductors, atomically thin  $\text{WS}_2$  is extremely sensitive to external chemical and gas environments and illumination conditions because of high surface-to-volume ratio.<sup>32–34</sup> The electrical characteristics and photoelectrical responses of a mechanically exfoliated ultrathin layer of  $\text{WS}_2$  can be affected by the adsorbents in ambient air. Gas doping can be an effective and easy technique for tuning the electrical properties of 2D materials.

In the present study, we demonstrated the improved device performance of exfoliated single-, bi-, and multi-layer  $\text{WS}_2$  FETs by using deep-ultraviolet (DUV) light in nitrogen ( $\text{N}_2$ ) and oxygen ( $\text{O}_2$ ) gas environments. The device performance of single-, bi-, and multi-layer  $\text{WS}_2$  FETs was investigated through electrical transport measurements, Raman spectroscopy, and photocurrent measurement. After illuminated by deep-ultraviolet (DUV) light in nitrogen ( $\text{N}_2$ ) gas environment,  $\text{WS}_2$  FET shows enhanced charge carrier density, mobility and photocurrent response, showing the n-type doping effect. The doping effect is reversible. The pristine characteristics of  $\text{WS}_2$  FET can be restored by DUV light illumination in oxygen ( $\text{O}_2$ ) gas environment.

## 2. Experimental Section

### 2.1. Sample preparation:

The exfoliated single-, bi-, and multi-layer WS<sub>2</sub> films were obtained from naturally occurring bulk crystals of WS<sub>2</sub> by transferring the films on a Si substrate with a 300 nm-thick SiO<sub>2</sub> capping layer using the standard scotch tape method. Structural morphology, thickness, and topography of the single-, bi-, and multi-layer WS<sub>2</sub> films were examined using optical microscopy, Raman spectroscopy, and AFM, respectively. The laser wavelength of the Raman micro-spectrometer was 514 nm, and power was kept below 1.0 mW to avoid laser-induced heating. The laser spot size of the Raman spectroscopy was 0.7 μm for a 514 nm wavelength.

### 2.2. Device fabrication and characterization

Single-, bi-, and multi-layer WS<sub>2</sub> devices were fabricated through photolithography, e-beam lithography, and O<sub>2</sub> plasma etching. Large electrode patterns with a Cr/Au (6/30 nm) film were deposited using a thermal evaporator after standard photolithography. E-beam lithography was then employed to pattern the source and drain electrodes, where the film was created through the evaporation of Cr/Au (10/80 nm). After device fabrication, all the devices were annealed in a tube furnace at a temperature of 300 °C in a flow of Ar/H<sub>2</sub> gas for four hours. Electrical transport measurements were carried out at room temperature under vacuum. Transport characteristics and Raman spectroscopy were also performed for WS<sub>2</sub> FETs after exposure to DUV with a dominant wavelength of  $\lambda = 220$  nm and an average intensity of 11 mW/cm<sup>2</sup> in a continuous N<sub>2</sub> or O<sub>2</sub> gas flow for a certain time.

### 3. Results and Discussion

#### 3.1. Optical and Atomic Force Microscopy

Figure 1a shows the schematic of a WS<sub>2</sub> FET device in the DUV light illumination setup with a gas flow. Air was evacuated, and then dry gas was introduced for the DUV treatment. Figures 1b, 1c, and 1d represent the optical images of the single-, bi-, and multi-layer WS<sub>2</sub> films with Cr/Au electrical contacts. The optical image shows different contrasts depending on the thickness of the WS<sub>2</sub> flake on the Si/SiO<sub>2</sub> substrate. The single-, bi-, and multi-layer WS<sub>2</sub> flakes were further verified through atomic force microscopy (AFM) and Raman spectra. Figure 2 shows the surface topologies of the single-, bi-, and multi-layer WS<sub>2</sub> films obtained by using AFM. The thickness profiles show that all the layers were quite smooth with very low roughness. All the scans were taken in tapping mode under ambient conditions, and the scan area was kept at 2×2 μm. The thickness of the single-layer WS<sub>2</sub> film was measured as 0.74 nm while the thickness of the bi-layer and multi-layer WS<sub>2</sub> films were measured as 1.43 and 3.55 nm respectively, indicating bi- and five-layer of WS<sub>2</sub> flakes.

#### 3.2. Electrical transport measurement in the pristine state

To check the electrical characteristics of the device, electrical transport measurement was performed at room temperature under vacuum. Figure 3a shows the transfer characteristics ( $I_{ds}$ - $V_{bg}$ ) of the single-layer WS<sub>2</sub> (SL-WS<sub>2</sub>) FET at a fixed source-drain voltage,  $V_{ds} = 1$  V. The black curve in the graph is plotted in the logarithmic scale for the  $I_{ds}$ - $V_{bg}$  curve. Output current on/off ratio of the SL-WS<sub>2</sub> FET was  $\approx 10^6$ , and threshold voltage ( $V_{th}$ ), which is defined as the intercept of the  $V_{bg}$  axis obtained by extrapolating the linear portion of the curve of  $I_{ds}$  versus  $V_{bg}$ ,<sup>35</sup> was around -1 V, suggesting a slight n-type doping in the pristine state. Output ( $I_{ds}$ - $V_{ds}$ ) characteristic curves at various gate voltages ranging from -10 V to +40 V in steps of 10 V for the SL-WS<sub>2</sub> FET are shown in Figure 3b. The nonlinear output ( $I_{ds}$ - $V_{ds}$ ) characteristics suggest the existence of Schottky barriers between Cr/Au metal

contact and WS<sub>2</sub> at the source and drain parts. Figure 3c represents the transfer characteristics ( $I_{ds}$ - $V_{bg}$ ) of the bi-layer WS<sub>2</sub> (BL-WS<sub>2</sub>) FET at  $V_{ds} = 1$  V. The output current on/off ratio for the BL-WS<sub>2</sub> FET is  $\approx 10^5$ , and the  $V_{th}$  was around -3 V, which also indicates n-type doping in the pristine state. Output ( $I_{ds}$ - $V_{ds}$ ) characteristic curves at various gate voltages ranging from -10 V to +40 V for the BL-WS<sub>2</sub> FET are shown in Figure 3d. Similarly, Figure 3e represents the transfer characteristics ( $I_{ds}$ - $V_{bg}$ ) for the multi-layer WS<sub>2</sub> (ML-WS<sub>2</sub>) FET. The output current on/off ratio of the ML-WS<sub>2</sub> FET was  $\approx 10^5$ . The typical output ( $I_{ds}$ - $V_{ds}$ ) characteristic curves at various gate voltages ranging from -10 V to +40 V for the ML-WS<sub>2</sub> FET are shown in Figure 3e. While hysteresis in threshold voltage of WS<sub>2</sub> FETs was around 6-8 V in the pristine state,<sup>36</sup> WS<sub>2</sub> FETs after DUV illumination in an N<sub>2</sub> gas environment do not show a considerable hysteresis during the repeated sweeps of back gate voltages ( $V_{bg}$ ), which demonstrates charging-effect-free devices after the DUV treatment (Figure S1 in Supporting Information).

### 3.3. Electrical transport measurement after DUV light illumination in the presence of nitrogen and oxygen gas

We then introduced a simple tuning method to enhance the charge carrier density and mobility. WS<sub>2</sub> FETs were exposed to DUV light for different periods in the presence of N<sub>2</sub> gas. The effect of DUV illumination in an N<sub>2</sub> gas environment (DUV+N<sub>2</sub>) was n-type doping, whereas a subsequent DUV illumination in an O<sub>2</sub> gas environment (DUV+O<sub>2</sub>) was dedoping of the n-type doped WS<sub>2</sub> FET. Figures 4a, 4c, and 4e show the respective transfer characteristics ( $I_{ds}$ - $V_{bg}$ ) of SL, BL, and ML-WS<sub>2</sub> FETs after DUV light illumination in N<sub>2</sub> and O<sub>2</sub> gas environments for different periods. The threshold voltage shifted toward negative gate voltages after DUV illumination in the N<sub>2</sub> gas, which revealed n-type doping for all WS<sub>2</sub> FETs. The output current  $I_{ds}$  of all WS<sub>2</sub> FETs increased after DUV+N<sub>2</sub> treatment, but was significantly reduced and  $V_{th}$  shifted toward positive gate voltages after DUV+O<sub>2</sub> treatment.

After the 30 min DUV+N<sub>2</sub> treatment, the output current on/off ratio remained in the same power range as that in the pristine state, which were  $\sim 10^6$  for SL-WS<sub>2</sub> FET,  $\sim 10^5$  for BL-WS<sub>2</sub> FET, and  $\sim 10^5$  for SL-WS<sub>2</sub> FET, as seen in Figure S3. Figures 4b, 4d, and 4f represent the change in  $V_{th}$  as a function of time of DUV+N<sub>2</sub> and DUV+O<sub>2</sub> treatments on SL-WS<sub>2</sub>, BL-WS<sub>2</sub>, and ML-WS<sub>2</sub> FETs, respectively. After the 30 min DUV+N<sub>2</sub> treatment,  $V_{th}$  reached -60, -53, and -48 V for SL-WS<sub>2</sub>, BL-WS<sub>2</sub>, and ML-WS<sub>2</sub> FETs respectively. After the subsequent treatment of 10 min DUV+O<sub>2</sub>,  $V_{th}$  was restored to similar values in the pristine states.

The n-type doping effect for WS<sub>2</sub> FETs by DUV light illumination in N<sub>2</sub> can be considered as the removal of O<sub>2</sub> molecules from WS<sub>2</sub> nanoflakes.<sup>35-37</sup> The oxygen atoms/molecules on the surface of WS<sub>2</sub> nanoflakes may work as acceptors to draw electrons in the WS<sub>2</sub> layer. Therefore, oxygen removal significantly increases the drain-to-source current in WS<sub>2</sub> nanoflakes. N<sub>2</sub> gas alone without DUV illumination does not affect the electrical properties of WS<sub>2</sub> FETs. An amount of energy is required to release oxygen from the surface of WS<sub>2</sub>.<sup>38,39</sup> DUV illumination provides the energy required for nitrogen atoms to react with oxygen atoms, which originally adhere to WS<sub>2</sub>. The DUV illumination in the oxygen gas environment shifted  $V_{th}$  toward positive gate voltages because the oxygen atoms/molecules adsorbed in sulfur or defect sites on the WS<sub>2</sub> surface trap electrons and reduce the number of charge carriers. Oxygen is adsorbed on a WS<sub>2</sub> flake surface in two ways. One, oxygen gas molecules can easily dissociate into oxygen atoms under the illumination of DUV light, and then dissociated oxygen atoms interact with WS<sub>2</sub>; and two, oxygen molecules can be directly adsorbed by WS<sub>2</sub> nanosheets. DUV light provides enough energy to facilitate oxygen adsorption onto the WS<sub>2</sub> surface. These results show that adsorbents play an important role in the electrical transport properties of WS<sub>2</sub> FETs.

WS<sub>2</sub> films were further examined by energy-dispersive x-ray (EDX) spectroscopy to verify the gas element adsorption. Changes in the amount of elements should be detected by EDX spectroscopy because DUV+N<sub>2</sub> treatment removes oxygen atoms or molecules adsorbed

on the surface of WS<sub>2</sub> films. The x-rays were scanned on a 500×500 nm<sup>2</sup> area centered on the WS<sub>2</sub> films to obtain the average value of atomic elements. The relative amounts of oxygen after DUV+N<sub>2</sub> treatment for SL-WS<sub>2</sub>, BL-WS<sub>2</sub>, and ML-WS<sub>2</sub> were reduced by 2.3±0.011%, 2.1±0.015%, and 1.9±0.013%, respectively. The background signal for oxygen, which mostly originated from a 300 nm-thick SiO<sub>2</sub> capping layer, was large. However, the reduced amount of oxygen was consistently observed after 30 min DUV+N<sub>2</sub> treatment for all devices (Table S1).

When TMDC devices are exposed with different gases, the change in conductance can normally result from two main factors: charge transfer and Schottky barrier modulation. Absorption of different gases can modify the Schottky barrier height and width. Specifically, oxygen absorption can shift the Fermi level of WS<sub>2</sub> toward the valence band. That can increase the height and width of the Schottky barrier and leads to decrease in device current. Influence of band bending on Schottky barrier height after p and n-type doping was explained for MoS<sub>2</sub> devices.<sup>40</sup> Due to surface dipole layer formation absorbed gas molecules can change the work function of metal electrodes and semiconducting materials as already reported.<sup>40</sup> In this sense, our DUV+O<sub>2</sub> treatment will provide electron-trapping absorbate groups (such as oxygen or an oxygen-derived group) and give rise to withdrawal of electrons from the channel materials resulting in the p-doping effect, which increases the Schottky barrier height. On the other hand, DUV+N<sub>2</sub> treatment will remove the electron-trapping absorbate groups from WS<sub>2</sub> flakes, causing the opposite trend in comparison with DUV+O<sub>2</sub> treatment.

One important factor for a tuning method to be applicable to FETs is to preserve the active channel without degradation. We examined the changes in mobility and carrier density after the DUV treatments. Figure 5 shows the field-effect mobilities and carrier densities of SL-WS<sub>2</sub>, BL-WS<sub>2</sub>, and ML-WS<sub>2</sub> FETs at room temperature as a function of time of DUV+N<sub>2</sub> and DUV+O<sub>2</sub> treatments. The field-effect mobilities of pristine SL-WS<sub>2</sub>, BL-WS<sub>2</sub>, and ML-WS<sub>2</sub> FETs were 4, 30, and 90 cm<sup>2</sup>/V, respectively. Field-effect mobility was obtained by

using the equation  $\mu = \frac{1}{C_g} \frac{L}{W} \left( \frac{dI_{ds}}{dV_{bg}} \right) \frac{1}{V_{ds}}$ ,<sup>41-43</sup> where  $L$  is the channel length,  $W$  is the channel width,  $\frac{dI_{ds}}{dV_{bg}}$  is the slope of transfer characteristic of the device with  $V_{ds} = 1$  V, and  $C_g$  is the gate capacitance of  $\sim 105$  aF/ $\mu\text{m}^2$  for the Si/SiO<sub>2</sub> substrate. The value of  $\frac{dI_{ds}}{dV_{bg}}$  is obtained by fitting the linear regime of the transfer characteristic curves of WS<sub>2</sub> FETs. Therefore, it is an average value of extrinsic transconductance  $g_{\text{ext}}$  rather than peak extrinsic transconductance  $g_m$ . The mobilities of the WS<sub>2</sub> FETs in pristine state were comparable to other 2D semiconductor materials like MoS<sub>2</sub>. However, the field-effect mobilities of the WS<sub>2</sub> FETs were significantly enhanced after DUV+N<sub>2</sub> treatment. After the 30 min DUV+N<sub>2</sub> treatment, the field-effect mobilities improved to 15, 47, and 125 cm<sup>2</sup>/V for SL-WS<sub>2</sub>, BL-WS<sub>2</sub>, and ML-WS<sub>2</sub> FETs, respectively. The mobilities were reduced to values near the pristine states after the 10 min DUV+O<sub>2</sub> treatment (Figures 5a, 5c, and 5e). The carrier densities of SL-WS<sub>2</sub>, BL-WS<sub>2</sub>, and ML-WS<sub>2</sub> FETs as a function of DUV exposure time in the N<sub>2</sub> and O<sub>2</sub> gas environments are respectively shown in Figures 4b, 4d, and 4f. Charge carrier densities ( $n$ ) of the devices were calculated by using the relation  $n = C_g (V_{bg} - V_{th}) / e$ ,<sup>41-43</sup> where  $V_{th}$  is the threshold voltage of the device, and  $e$  is the electronic charge. Figures 5b, 5d, and 5f show the charge carrier densities for the WS<sub>2</sub> FETs for  $V_{bg} = +30$  V at  $T = 300$  K. The carrier densities of SL-WS<sub>2</sub>, BL-WS<sub>2</sub>, and ML-WS<sub>2</sub> FETs notably increased after DUV+N<sub>2</sub> treatment and returned to the pristine state after DUV+O<sub>2</sub> treatment (Figures 5b, 5d, and 5f).

### 3.4. Raman Spectra measurement for different number of WS<sub>2</sub> layers

Structural characterizations of the SL-WS<sub>2</sub>, BL-WS<sub>2</sub>, and ML-WS<sub>2</sub> films were performed through Raman spectroscopy. Figure 6a shows a Raman shift taken for pristine SL-WS<sub>2</sub>, BL-WS<sub>2</sub>, and ML-WS<sub>2</sub> films in FETs. Raman spectra of the SL-WS<sub>2</sub>, BL-WS<sub>2</sub>, and

ML-WS<sub>2</sub> films showed strong signals of in-plane E<sub>2g</sub><sup>1</sup>, out-of-plane A<sub>1g</sub>, and vibration second-order 2LA(M) modes. The first-order E<sub>2g</sub><sup>1</sup> and A<sub>1g</sub> optical modes were considered to explain the properties of 2D material, such as MoS<sub>2</sub>, in the previous report,<sup>44</sup> but the intensity of the 2LA(M) mode at 352 cm<sup>-1</sup> was distinctly predominant for WS<sub>2</sub>. Although the 2LA(M) mode overlapped with the first-order E<sub>2g</sub><sup>1</sup> mode at 355.4 cm<sup>-1</sup>, the multi-peak Lorentzian fitting can clarify their individual contributions as seen in Figure 6b. Figure 6c shows the detailed peak positions of E<sub>2g</sub><sup>1</sup>, A<sub>1g</sub>, and 2LA(M) modes depending on the number of layers. As the number of layers increases, the A<sub>1g</sub> mode shifts toward a higher wave number (blue shift), whereas the E<sub>2g</sub><sup>1</sup> and 2LA(M) phonon modes shift slightly toward a lower wave number (red shift). The wave number difference between these three Raman modes depends on the WS<sub>2</sub> film thickness, and can thus be used as an indicator of the number of layers. The Raman peak positions of E<sub>2g</sub><sup>1</sup> and A<sub>1g</sub> for SL-WS<sub>2</sub> are 355.4 and 417.4 cm<sup>-1</sup> respectively. The frequency difference between Raman A<sub>1g</sub> and E<sub>2g</sub><sup>1</sup> modes ( $\Delta = A_{1g} - E_{2g}^1$ ) is about 62.5 cm<sup>-1</sup>, which indicates a single layer of WS<sub>2</sub> film. For the BL-WS<sub>2</sub> device, E<sub>2g</sub><sup>1</sup> and A<sub>1g</sub> are located at 355 and 418.5 cm<sup>-1</sup>, respectively, and  $\Delta = 63.4$  cm<sup>-1</sup>, indicating two layers of WS<sub>2</sub> film. Finally for ML-WS<sub>2</sub>, E<sub>2g</sub><sup>1</sup> and A<sub>1g</sub> are located at 354.7 and 420.2 cm<sup>-1</sup> respectively, and  $\Delta = 65.5$  cm<sup>-1</sup>, indicating multiple layers of WS<sub>2</sub> film. The wave number difference between 2LA(M) and A<sub>1g</sub> modes can also be used to identify the layer number of a WS<sub>2</sub> film. The wave number differences between 2LA(M) and A<sub>1g</sub> modes are 65.4, 68.4, and 70.2 cm<sup>-1</sup> for SL-WS<sub>2</sub>, BL-WS<sub>2</sub>, and ML-WS<sub>2</sub> films in the devices.

Raman peak intensity ratio and full width at half maximum (FWHM) are also known to depend on the WS<sub>2</sub> film thickness.<sup>25,41</sup> Figure 6d shows the intensity ratios of 2LA(M) and A<sub>1g</sub> for SL-WS<sub>2</sub>, BL-WS<sub>2</sub>, and ML-WS<sub>2</sub> films. The intensity ratio decreases as the number of WS<sub>2</sub> layers increases, demonstrating that the intensity ratio of  $I_{2LA}/I_{A1g}$  can also be used as an indicator of WS<sub>2</sub> film thickness.  $I_{2LA}/I_{A1g}$  was 2.1, 1.1, and 0.45 for SL-WS<sub>2</sub>, BL-WS<sub>2</sub>, and

ML-WS<sub>2</sub> films, respectively. Figure 6e shows the FWHM of E<sub>2g</sub><sup>1</sup> and A<sub>1g</sub> peaks for SL-WS<sub>2</sub>, BL-WS<sub>2</sub>, and ML-WS<sub>2</sub> films. FWHM decreases as the number of WS<sub>2</sub> layers is decreased. All observations in Raman spectra for the SL-WS<sub>2</sub>, BL-WS<sub>2</sub>, and ML-WS<sub>2</sub> films are consistent with the previous report.<sup>29,40,41</sup>

The doping effects by DUV+N<sub>2</sub> treatment are further examined through Raman spectroscopy. Figure 6f shows the Raman spectra of the SL-WS<sub>2</sub>, BL-WS<sub>2</sub>, and ML-WS<sub>2</sub> films after the 30 min DUV+N<sub>2</sub> treatment. A<sub>1g</sub> peak shifted from 417.4 cm<sup>-1</sup> to 413.6 cm<sup>-1</sup> for SL-WS<sub>2</sub>, from 418.5 cm<sup>-1</sup> to 415.1 cm<sup>-1</sup> for BL-WS<sub>2</sub>, and from 420.2 cm<sup>-1</sup> to 418.4 cm<sup>-1</sup> for ML-WS<sub>2</sub>. By contrast, E<sub>2g</sub><sup>1</sup> peak shifted downwards for a small amount of wave number: 1.7 cm<sup>-1</sup> for SL-WS<sub>2</sub>, 1.5 cm<sup>-1</sup> for BL-WS<sub>2</sub>, and 1.1 cm<sup>-1</sup> for ML-WS<sub>2</sub>. These results clearly indicate that the A<sub>1g</sub> vibration mode is sensitive to n-type doping by DUV+N<sub>2</sub> treatment and that the E<sub>2g</sub><sup>1</sup> is less affected. The A<sub>1g</sub> phonon couples strongly with electrons, and the A<sub>1g</sub> Raman peak softens and broadens with the increase of electron doping, whereas the E<sub>2g</sub><sup>1</sup> Raman peak weakly depends on the doping.<sup>45</sup> Furthermore, FWHMs of the A<sub>1g</sub> and E<sub>2g</sub><sup>1</sup> peaks were increased for all WS<sub>2</sub> films after the 30 min DUV+N<sub>2</sub> treatment.

An important question that arises is if a chemical reaction takes place and new compounds are formed during DUV illumination in gas environments. Raman spectroscopy was performed in a wide wave number range, from 200 cm<sup>-1</sup> to 1000 cm<sup>-1</sup>, to check the possible formation of tungsten trioxide (WO<sub>3</sub>). Several strong Raman peaks at 709 and 804 cm<sup>-1</sup> were expected for WO<sub>3</sub> to exist.<sup>46,47</sup> However, no Raman peaks were observed at such values for DUV+O<sub>2</sub> and DUV+N<sub>2</sub> treatments (Figure S4). Raman spectroscopy revealed that irreversible chemical reactions did not take place in the WS<sub>2</sub> films during DUV+O<sub>2</sub> and DUV+N<sub>2</sub> treatments.

In this experiment, DUV-driven doping is simple and easy to apply to already-made WS<sub>2</sub> FETs. However, for practical applications, the doping should be stable in an atmospheric environment. The transfer characteristics of SL-WS<sub>2</sub>, BL-WS<sub>2</sub>, and ML-WS<sub>2</sub> FETs were

measured after the films were left in an atmospheric environment for seven days after DUV+N<sub>2</sub> or DUV+O<sub>2</sub> treatment. Figure 7a reflects the very slight changes in output current and  $V_{th}$  of WS<sub>2</sub> FETs seven days after the 30 min DUV+N<sub>2</sub> treatment. Similarly, no significant change was observed in WS<sub>2</sub> FETs seven days after the 10 min DUV+O<sub>2</sub> treatment. Therefore, the doping of WS<sub>2</sub> by DUV illumination in gas environments is a simple yet sustainable method.

### 3.5. Photo-electrical measurement under Deep-Ultraviolet light

Owing to a well-developed bandgap, WS<sub>2</sub> FETs can also be used as optoelectronic devices. The optoelectronic response of WS<sub>2</sub> FETs in the vacuum by a 220 nm wavelength dominant DUV light was measured. A constant bias voltage of 1 V was applied between the source and the drain of the WS<sub>2</sub> FET, and  $I_{ds}$  was monitored for optoelectronic response. Photocurrent ( $I_{ph}$ ) is defined as the difference of  $I_{ds}$  with and without light illumination environment.<sup>48,49</sup> Figure 8a shows the photocurrent for SL-WS<sub>2</sub> FET before and after DUV+N<sub>2</sub> treatment. The photocurrent of SL-WS<sub>2</sub> FET was enhanced about four times after DUV+N<sub>2</sub> treatment. The enhancement was due to the improvement in electron mobility and increment of carrier density by the DUV+N<sub>2</sub> treatment, as shown in Figure 5. A large enhancement of the photocurrent was also found in BL-WS<sub>2</sub> and ML-WS<sub>2</sub> FETs after DUV+N<sub>2</sub> treatment, as shown in Figures 8b and 8c.

## 4. Conclusion

In summary, a simple yet sustainable doping method was developed to drastically improve the electrical and photoelectric characteristics of SL-WS<sub>2</sub>, BL-WS<sub>2</sub>, and ML-WS<sub>2</sub> FETs. Electrical transport measurement and Raman spectroscopy confirmed that the WS<sub>2</sub> FETs showed enhancements in charge carrier mobility, carrier density, and photocurrent response after DUV illumination in an N<sub>2</sub> environment. The n-type doping effect was

confirmed by the observations that the threshold voltage of the WS<sub>2</sub> FETs shifted toward the negative gate voltage and the positions of the E<sub>2g</sub><sup>1</sup> and A<sub>1g</sub> peaks in the Raman spectra shifted toward a lower wave number. This n-type doping by DUV illumination in an N<sub>2</sub> environment also enhanced the photocurrent in WS<sub>2</sub> FETs. The n-type doping effect is reversible. The pristine characteristics of WS<sub>2</sub> FET can be restored through DUV light illumination in an O<sub>2</sub> environment. The DUV-driven doping under a gas environment provides a very stable, effective, and easy-to-apply method to enhance the performance of a WS<sub>2</sub> FET.

### **Acknowledgements**

This research was supported by Nano-Material Technology Development Program (2012M3A7B4049888) through the National Research Foundation of Korea (NRF) funded by the Ministry of Science, ICT and Future Planning. This research was also supported by Priority Research Center Program (2010-0020207) and the Basic Science Research Program (2013R1A1A2061396) through NRF funded by the Ministry of Education.

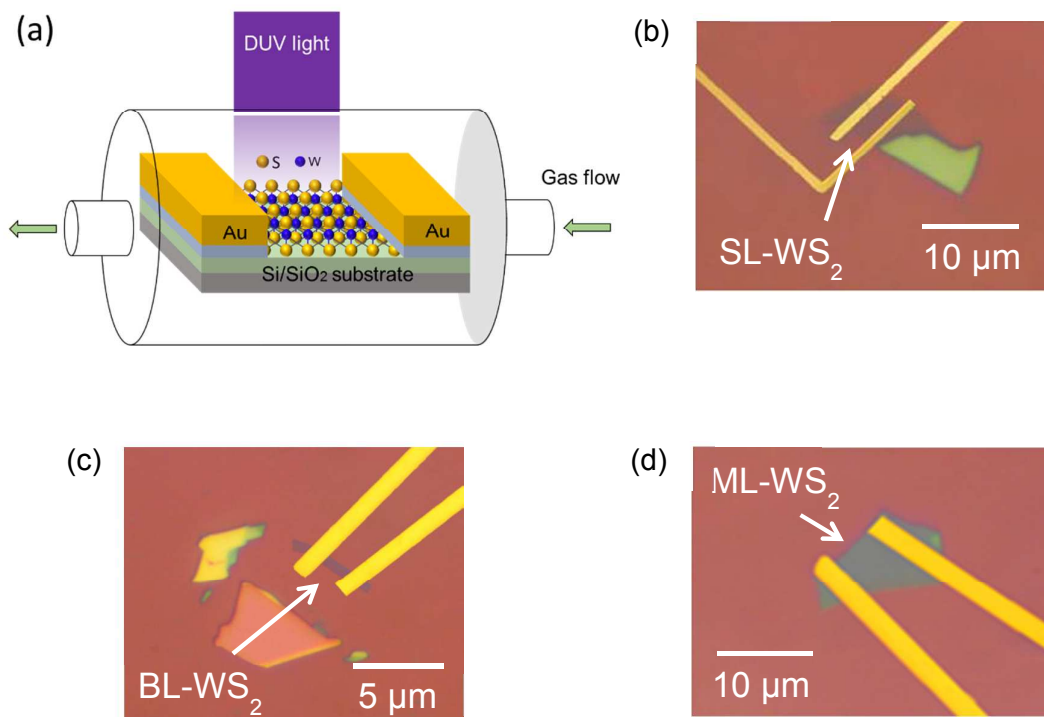


**Figure 1.** (a) Schematic of a WS<sub>2</sub> FET with DUV light illumination. (b) Optical image of the mechanically exfoliated monolayer, (c) bilayer, and (d) multi-layer WS<sub>2</sub> films on Si/SiO<sub>2</sub> substrate with source-drain contacts.

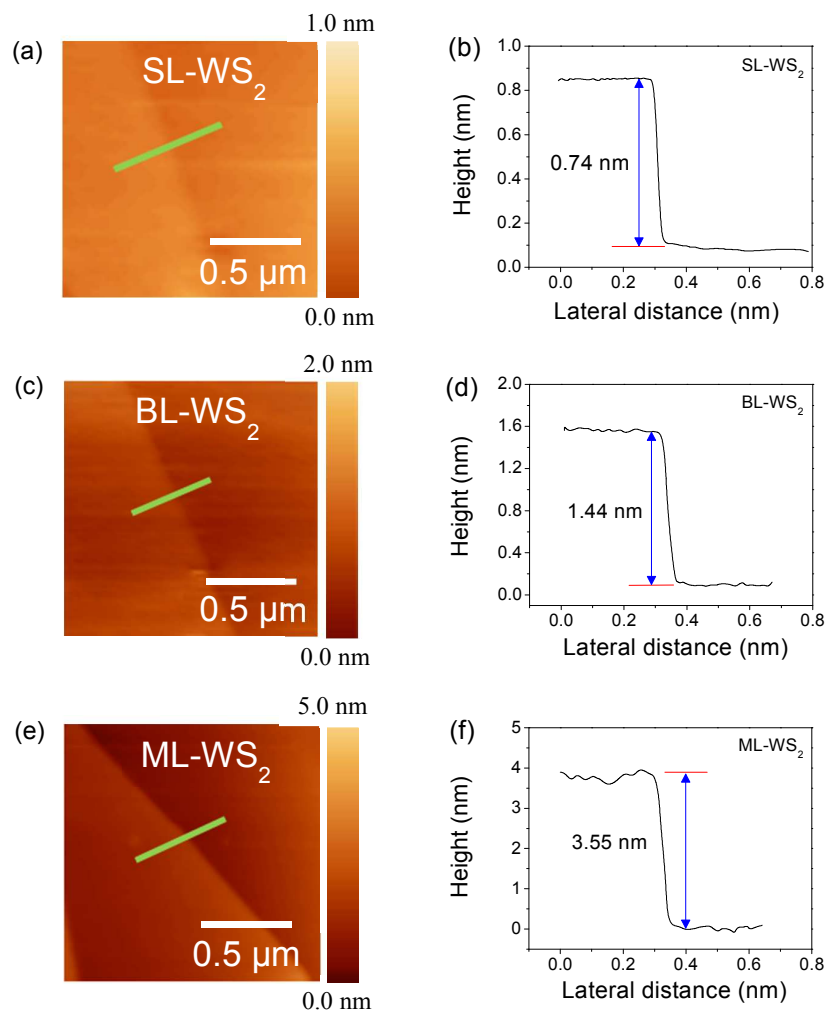


**Figure 2.** (a) Atomic force microscopy (AFM) image of single-layer WS<sub>2</sub> flake. (b) Height profile of the single-layer WS<sub>2</sub> along the green line in AFM image. The 0.74 nm thickness indicates one layer of WS<sub>2</sub> film. (c) AFM image of bilayer WS<sub>2</sub> flake. (d) Height profile of the bilayer WS<sub>2</sub> along the green line in AFM image. The 1.44 nm thickness indicates two layers of WS<sub>2</sub> film. (e) AFM image of multi-layer WS<sub>2</sub> flake. (f) Height profile of the multi-layer WS<sub>2</sub> along the green line in AFM image. The 3.55 nm thickness indicates five layers of WS<sub>2</sub> film.

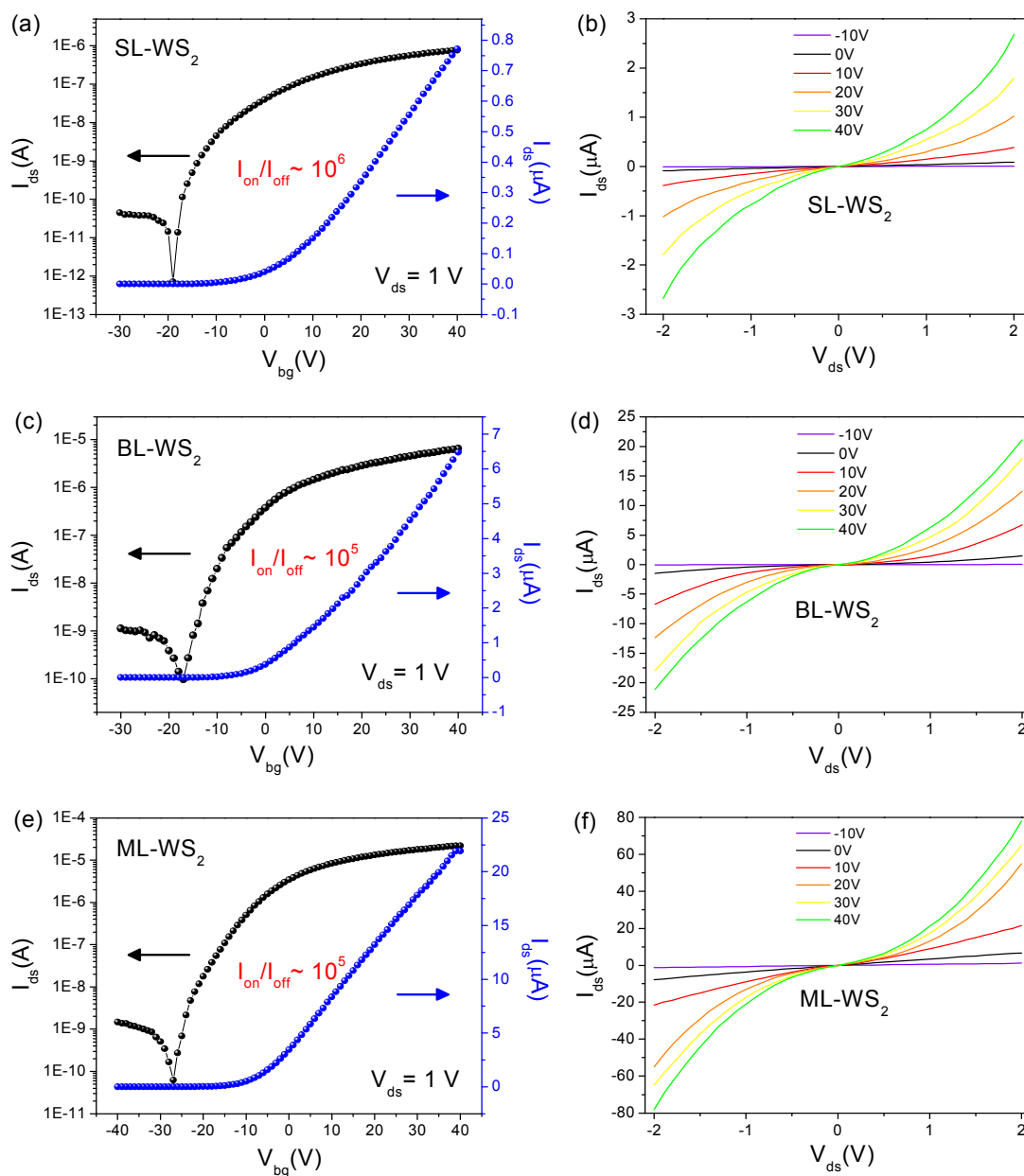


**Figure 3.** (a) Transfer characteristics ( $I_{ds}$ - $V_{bg}$ ) of the pristine SL-WS<sub>2</sub> FET. On/Off ratio of the device is  $\sim 10^6$ . (b) Output characteristics ( $I_{ds}$ - $V_{ds}$ ) of SL-WS<sub>2</sub> FET at different back gate voltages ranging from -10 V to +40 V in steps of 10 V. (c) Transfer characteristics ( $I_{ds}$ - $V_{bg}$ ) of the pristine BL-WS<sub>2</sub> FET. On/Off ratio of the device is  $\sim 10^5$ . (d) Output characteristics ( $I_{ds}$ - $V_{ds}$ ) of BL-WS<sub>2</sub> FET at different back gate voltages. (e) Transfer characteristics ( $I_{ds}$ - $V_{bg}$ ) of

the pristine ML-WS<sub>2</sub> FET. On/Off ratio of the device is  $\sim 10^5$ . (f) Output characteristics ( $I_{ds}$ - $V_{ds}$ ) of ML-WS<sub>2</sub> FET at different back gate voltages. All measurements were performed in vacuum at T = 300 K.

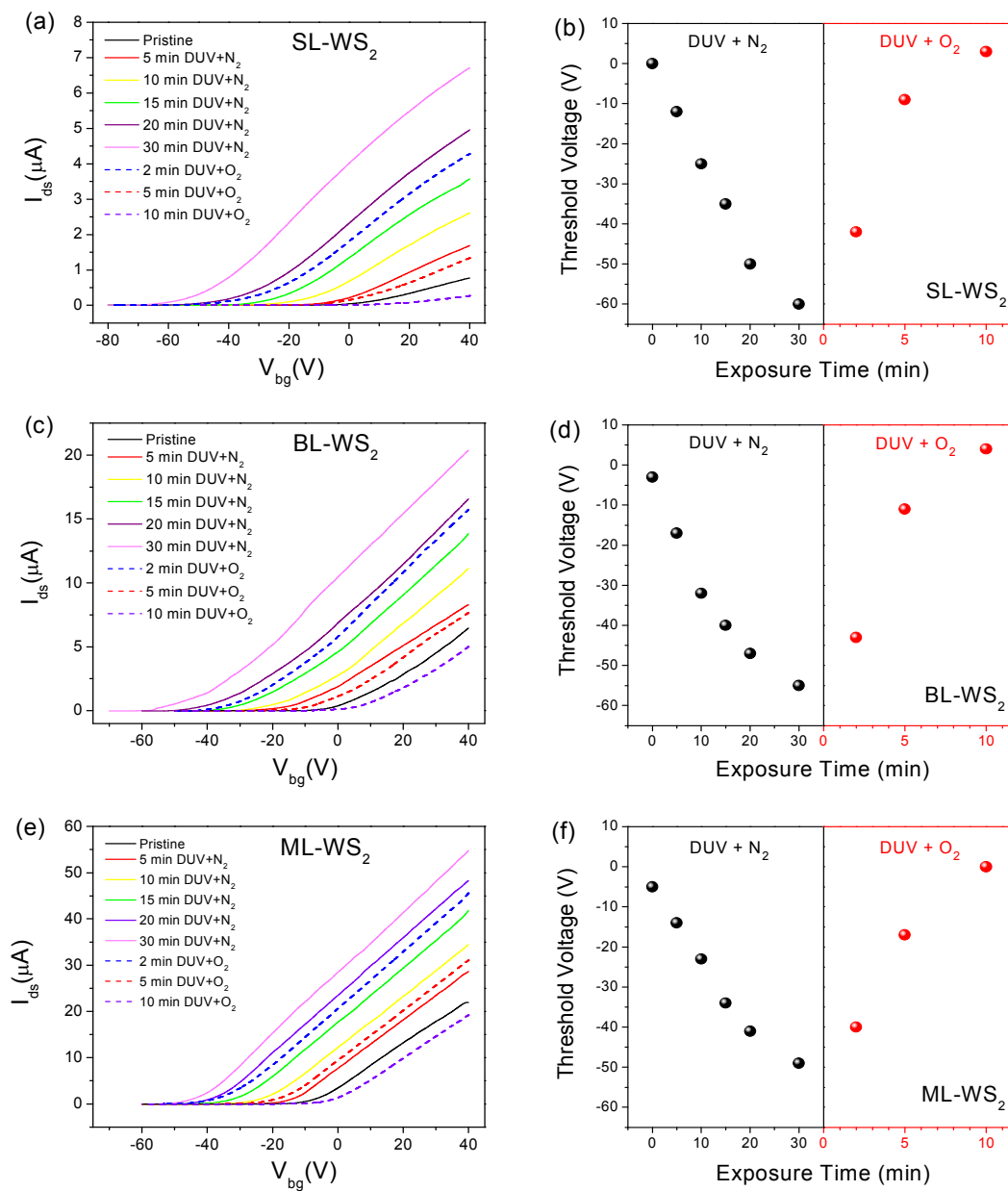


**Figure 4.** Doping of WS<sub>2</sub> layers by DUV+N<sub>2</sub> and DUV+O<sub>2</sub> treatments. (a) Transfer characteristics ( $I_{ds}$ - $V_{bg}$ ) of SL-WS<sub>2</sub> FET for different times of treatment by DUV+N<sub>2</sub> and DUV+O<sub>2</sub>. (b) Threshold voltage as a function of exposure time by DUV+N<sub>2</sub> and DUV+O<sub>2</sub> treatments for SL-WS<sub>2</sub> FET. (c) Transfer characteristics ( $I_{ds}$ - $V_{bg}$ ) of BL-WS<sub>2</sub> FET. (d) Threshold voltage as a function of exposure time for BL-WS<sub>2</sub> FET. (e) Transfer

characteristics ( $I_{ds}$ - $V_{bg}$ ) of ML-WS<sub>2</sub> FET. (f) Threshold voltage as a function of exposure time for ML-WS<sub>2</sub> FET. All measurements were performed in vacuum at T = 300 K.

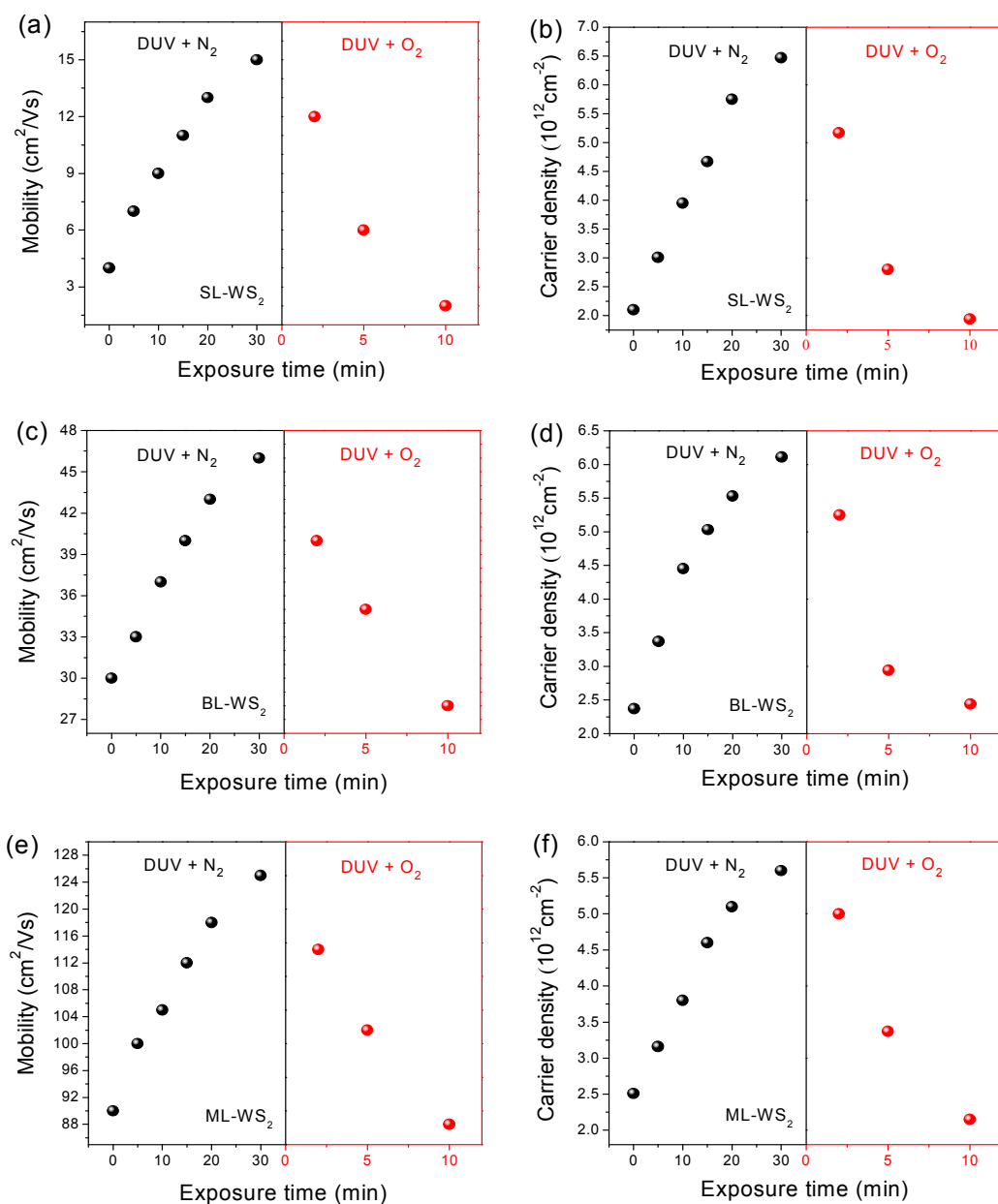


**Figure 5.** (a) Electron mobility as a function of exposure time by DUV+N<sub>2</sub> and DUV+O<sub>2</sub> treatments for SL-WS<sub>2</sub> FET. (b) Charge carrier density as a function of exposure time by DUV+N<sub>2</sub> and DUV+O<sub>2</sub> treatments for SL-WS<sub>2</sub> FET. (c) Electron mobility as a function of exposure time by DUV+N<sub>2</sub> and DUV+O<sub>2</sub> treatments for BL-WS<sub>2</sub> FET. (d) Charge carrier density as a function of exposure time by DUV+N<sub>2</sub> and DUV+O<sub>2</sub> treatments for BL-WS<sub>2</sub> FET. (e) Electron mobility as a function of exposure time by DUV+N<sub>2</sub> and DUV+O<sub>2</sub> treatments for ML-WS<sub>2</sub> FET. (f) Charge carrier density as a function of exposure time by DUV+N<sub>2</sub> and DUV+O<sub>2</sub> treatments for ML-WS<sub>2</sub> FET.

(e) Electron mobility as a function of exposure time by DUV+N<sub>2</sub> and DUV+O<sub>2</sub> treatments for ML-WS<sub>2</sub> FET. (f) Charge carrier density as a function of exposure time by DUV+N<sub>2</sub> and DUV+O<sub>2</sub> treatments for ML-WS<sub>2</sub> FET. The charge carrier densities were obtained for  $V_{bg} = +30$  V at T = 300 K.

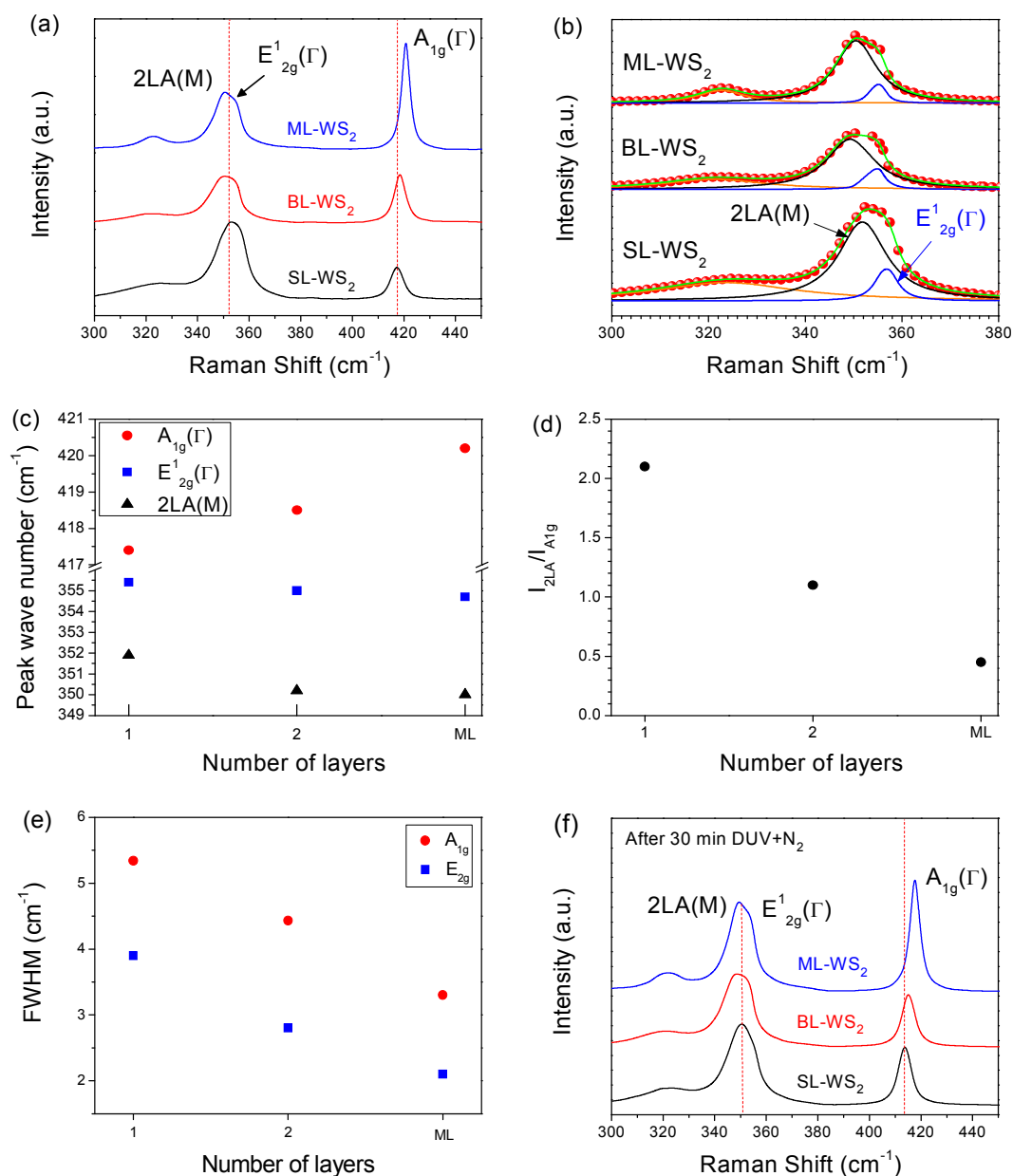


**Figure 6.** Raman spectra for monolayer (SL), bilayer (BL), and multi-layer (ML) WS<sub>2</sub> films using a laser with 514 nm wavelength. (a) Raman spectra for SL-WS<sub>2</sub>, BL-WS<sub>2</sub>, and ML-WS<sub>2</sub> in the pristine state. (b) Lorentzian fitting for E<sub>2g</sub> and 2LA(M) peaks. Red circles represent experimental data, while blue, black, and green lines represent E<sub>2g</sub>, 2LA(M), and combined peak fitting, respectively. (c) Raman peak wave number for SL-WS<sub>2</sub>, BL-WS<sub>2</sub>, and ML-WS<sub>2</sub>.

The  $A_{1g}$  peak shows a blue shift with an increasing number of  $WS_2$  layers, whereas the  $E_{2g}$  and  $2LA(M)$  peaks show a red shift. (d) Intensity ratio ( $I_{2LA(M)}/I_{A_{1g}}$ ) for SL- $WS_2$ , BL- $WS_2$ , and ML- $WS_2$  films. Intensity ratio decreases with the increasing number of  $WS_2$  layers. (e) FWHM of  $A_{1g}$  and  $E_{2g}$  for SL- $WS_2$ , BL- $WS_2$ , and ML- $WS_2$  films. FWHM of  $A_{1g}$  and  $E_{2g}$  peaks decreases with the increasing number of  $WS_2$  layers. (f) Raman spectra of SL- $WS_2$ , BL- $WS_2$ , and ML- $WS_2$  films after exposure to the 30 min DUV+N<sub>2</sub> treatment.

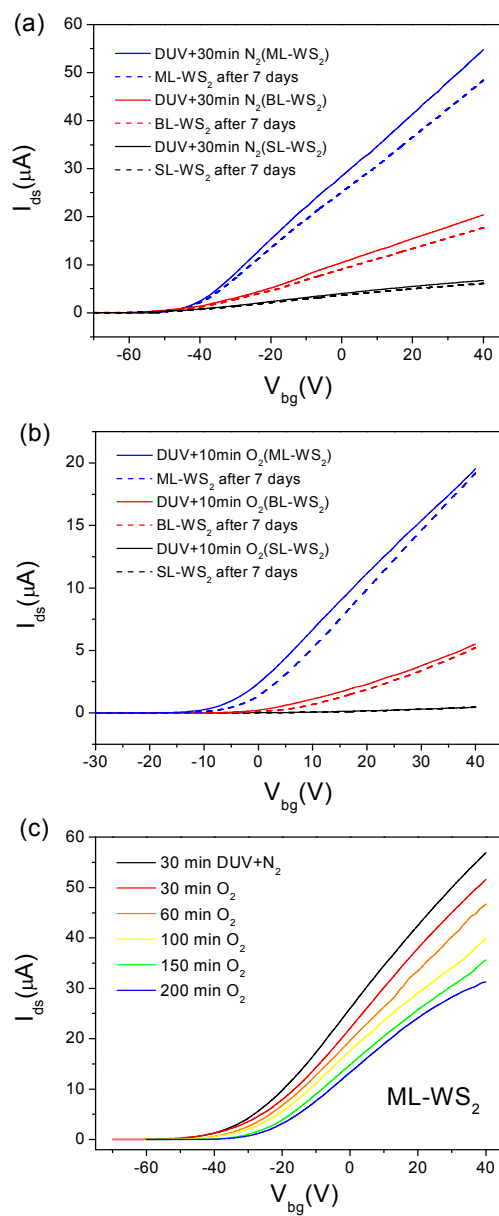


**Figure 7.** (a) Transfer characteristics ( $I_{ds}$ - $V_{bg}$ ) of SL-WS<sub>2</sub>, BL-WS<sub>2</sub>, and ML-WS<sub>2</sub> FETs seven days after the 30 min DUV+N<sub>2</sub> treatment. (b) Transfer characteristics ( $I_{ds}$ - $V_{bg}$ ) of SL-WS<sub>2</sub>, BL-WS<sub>2</sub>, and ML-WS<sub>2</sub> FETs seven days after the 30 min DUV+O<sub>2</sub> treatment. (c) Transfer characteristics ( $I_{ds}$ - $V_{bg}$ ) of ML-WS<sub>2</sub> FETs after exposure to O<sub>2</sub> gas flow for a certain time without DUV.

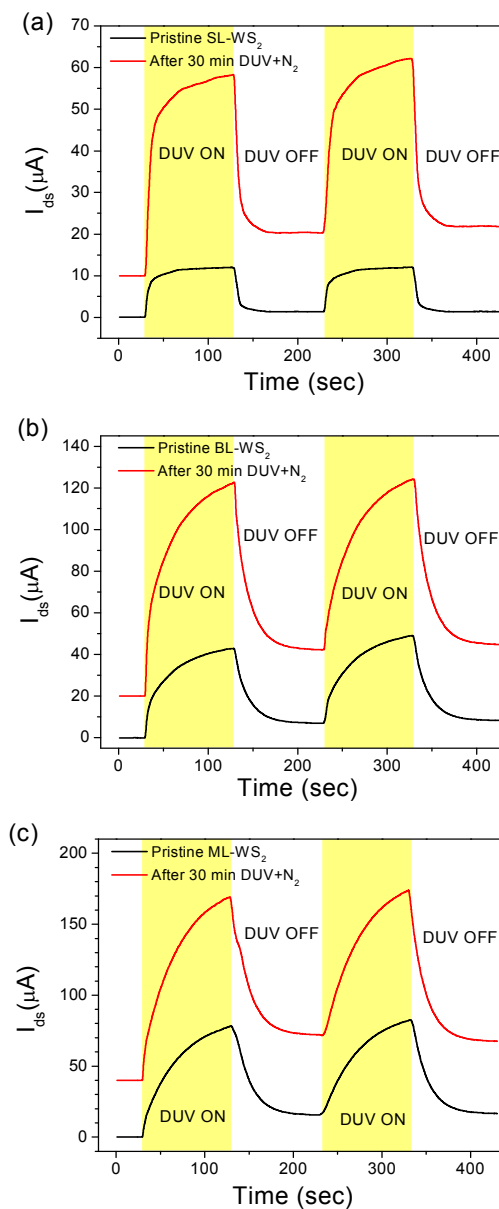


**Figure 8.** Photocurrent response of the WS<sub>2</sub> FET by 220 nm wavelength dominant DUV illumination before and after the 30 min DUV+N<sub>2</sub> treatment. A constant bias voltage of 1 V was applied between the source and the drain of the WS<sub>2</sub> FET, and  $I_{ds}$  was monitored for photocurrent response. All measurements were performed in vacuum at  $T = 300$  K. Plots are shifted for clarity. (a) DUV-driven  $I_{ds}$  of SL-WS<sub>2</sub> FET before (black line) and after (red line) DUV+N<sub>2</sub> treatment. (b) DUV-driven  $I_{ds}$  of BL-WS<sub>2</sub> FET before (black line) and after (red

line) DUV+N<sub>2</sub> treatment. (c) DUV-driven  $I_{ds}$  of ML-WS<sub>2</sub> FET before (black line) and after (red line) DUV+N<sub>2</sub> treatment.

**References**

1. A. K. Geim and K. S. Novoselov, *Nat Mater*, 2007, **6**, 183-191.
2. J. Choi, H. Kim, J. Park, M. W. Iqbal, M. Z. Iqbal, J. Eom and J. Jung, *Current Applied Physics*, 2014,**14**,1045-1050.
3. C. Lee, X. Wei, J. W. Kysar and J. Hone, *Science*, 2008, **321**, 385-388.
4. H. Chen, M. B. Müller, K. J. Gilmore, G. G. Wallace and D. Li, *Adv Mater*, 2008, **20**, 3557-3561.
5. S. Vadukumpully, J. Paul, N. Mahanta and S. Valiyaveetil, *Carbon*, 2011, **49**, 198-205.
6. M. Iqbal, M. F. Khan, M. W. Iqbal and J. Eom, *J. Mater. Chem. C*, 2014, **2**, 5404-5410.
7. B. Zhang and T. Cui, *Applied Physics Letters*, 2011, **98**, 073116.
8. M. Z. Iqbal, M. W. Iqbal, J. H. Lee, Y. S. Kim, S.-H. Chun and J. Eom, *Nano Research*, 2013, **6**, 373-380.
9. M. Iqbal, A. K. Singh, M. Iqbal, S. Seo and J. Eom, *Journal of Applied Physics*, 2012, **111**, 084307.
10. M. Iqbal, A. K. Singh, M. Iqbal and J. Eom, *Journal of Physics: Condensed Matter*, 2012, **24**, 335301.
11. M. Iqbal, O. Kelekci, M. Iqbal and J. Eom, *Carbon*, 2013, **59**, 366-371.
12. M. Y. Han, B. Özyilmaz, Y. Zhang and P. Kim, *Phys Rev Lett*, 2007, **98**, 206805.
13. D. Li and R. B. Kaner, *Science*, 2008, **320**, 1170-1171.
14. R. Balog, B. Jørgensen, L. Nilsson, M. Andersen, E. Rienks, M. Bianchi, M. Fanetti, E. Lægsgaard, A. Baraldi and S. Lizzit, *Nat Mater*, 2010, **9**, 315-319.
15. T. Ohta, A. Bostwick, T. Seyller, K. Horn and E. Rotenberg, *Science*, 2006, **313**, 951-954.
16. J. B. Oostinga, H. B. Heersche, X. Liu, A. F. Morpurgo and L. M. Vandersypen, *Nat*

- Mater*, 2007, **7**, 151-157.
17. B. Radisavljevic, A. Radenovic, J. Brivio, V. Giacometti and A. Kis, *Nat Nanotechnol*, 2011, **6**, 147-150.
  18. T. Georgiou, R. Jalil, B. D. Belle, L. Britnell, R. V. Gorbachev, S. V. Morozov, Y.-J. Kim, A. Gholinia, S. J. Haigh and O. Makarovskiy, *Nat Nanotechnol*, 2013, **8**, 100-103.
  19. H. Fang, M. Tosun, G. Seol, T. C. Chang, K. Takei, J. Guo and A. Javey, *Nano Lett*, 2013, **13**, 1991-1995.
  20. D. Braga, I. Gutiérrez Lezama, H. Berger and A. F. Morpurgo, *Nano Lett*, 2012, **12**, 5218-5223.
  21. H. Li, Z. Yin, Q. He, H. Li, X. Huang, G. Lu, D. W. H. Fam, A. I. Y. Tok, Q. Zhang and H. Zhang, *Small*, 2012, **8**, 63-67.
  22. H. Fang, S. Chuang, T. C. Chang, K. Takei, T. Takahashi and A. Javey, *Nano Lett*, 2012, **12**, 3788-3792.
  23. S. Kim, A. Konar, W.-S. Hwang, J. H. Lee, J. Lee, J. Yang, C. Jung, H. Kim, J.-B. Yoo and J.-Y. Choi, *Nature communications*, 2012, **3**, 1011.
  24. S. Jo, N. Ubrig, H. Berger, A. B. Kuzmenko and A. F. Morpurgo, *Nano Lett*, 2014, **14**, 2019-2025.
  25. A. Berkdemir, H. R. Gutiérrez, A. R. Botello-Méndez, N. Perea-López, A. L. Elías, C.-I. Chia, B. Wang, V. H. Crespi, F. López-Urías and J.-C. Charlier, *Scientific reports*, 2013, **3**, 1755.
  26. H. Zeng, G.-B. Liu, J. Dai, Y. Yan, B. Zhu, R. He, L. Xie, S. Xu, X. Chen and W. Yao, *Scientific reports*, 2013, **3**, 1608.
  27. W. Zhao, Z. Ghorannevis, L. Chu, M. Toh, C. Kloc, P.-H. Tan and G. Eda, *Acs Nano*, 2012, **7**, 791-797.
  28. T. Georgiou, H. Yang, R. Jalil, J. Chapman, K. S. Novoselov and A. Mishchenko,

- Dalton Transactions*, **2014**, DOI: 10.1039/C3DT52353E.
29. W. Zhao, Z. Ghorannevis, K. K. Amara, J. R. Pang, M. Toh, X. Zhang, C. Kloc, P. H. Tan and G. Eda, *Nanoscale*, 2013, **5**, 9677-9683.
  30. M. M. Perera, M.-W. Lin, H.-J. Chuang, B. P. Chamlagain, C. Wang, X. Tan, M. M.-C. Cheng, D. Tománek and Z. Zhou, *Acs Nano*, 2013, **7**, 4449-4458.
  31. D.-S. Tsai, K.-K. Liu, D.-H. Lien, M.-L. Tsai, C.-F. Kang, C.-A. Lin, L.-J. Li and J.-H. He, *Acs Nano*, 2013, **7**, 3905-3911.
  32. H. Liu, A. T. Neal and P. D. Ye, *Acs Nano*, 2012, **6**, 8563-8569.
  33. S. Das, H.-Y. Chen, A. V. Penumatcha and J. Appenzeller, *Nano Lett*, 2012, **13**, 100-105.
  34. D. Jariwala, V. K. Sangwan, L. J. Lauhon, T. J. Marks and M. C. Hersam, *Acs Nano*, 2014, **8**, 1102-1120.
  35. W. Park, J. Park, J. Jang, H. Lee, H. Jeong, K. Cho, S. Hong and T. Lee, *Nanotechnology*, 2013, **24**, 095202.
  36. D. J. Late, B. Liu, H. R. Matte, V. P. Dravid and C. Rao, *Acs Nano*, 2012, **6**, 5635-5641.
  37. Q. Yue, Z. Shao, S. Chang and J. Li, *Nanoscale research letters*, 2013, **8**, 1-7.
  38. M. Iqbal, S. Siddique, M. Iqbal and J. Eom, *J. Mater. Chem. C*, 2013, **1**, 3078-3083.
  39. M. W. Iqbal, M. Z. Iqbal, X. Jin, C. Hwang and J. Eom, *ACS applied materials & interfaces*, 2014, **6**, 4207-4213.
  40. B. Liu, L. Chen, G. Liu, A. N. Abbas, M. Fathi and C. Zhou, *Acs Nano*, 2014, **8**, 5304-5314.
  41. Y. Zhan, Z. Liu, S. Najmaei, P. M. Ajayan and J. Lou, *Small*, 2012, **8**, 966-971.
  42. Y.-H. Lee, L. Yu, H. Wang, W. Fang, X. Ling, Y. Shi, C.-T. Lin, J.-K. Huang, M.-T. Chang and C.-S. Chang, *Nano Lett*, 2013, **13**, 1852-1857.
  43. J. D. Lin, C. Han, F. Wang, R. Wang, D. Xiang, S. Q. Qin, X. A. Zhang, L. Wang, H.

- Zhang, A. T. S. Wee and W. Chen, *Acs Nano*, 2014, **8**, 5323-5329.
44. H. Li, Q. Zhang, C. C. R. Yap, B. K. Tay, T. H. T. Edwin, A. Olivier and D. Baillargeat, *Adv Funct Mater*, 2012, **22**, 1385-1390.
45. J. D. Lin, C. Han, F. Wang, R. Wang, D. Xiang, S. Qin, X.-A. Zhang, L. Wang, H. Zhang and A. T. S. Wee, *Acs Nano*, 2014, **8**, 5323-5329.
46. M. Ostromecki, I. E. Wachs, S. D. Kohler and J. G. Ekerdt, *Catalysis letters*, 1995, **33**, 209-215.
47. G. Ramāns, J. Gabrusenoks and A. Veispāls, *physica status solidi (a)*, 1982, **74**, K41-K44.
48. Z. Yin, H. Li, H. Li, L. Jiang, Y. Shi, Y. Sun, G. Lu, Q. Zhang, X. Chen and H. Zhang, *Acs Nano*, 2011, **6**, 74-80.
49. O. Lopez-Sanchez, D. Lembke, M. Kayci, A. Radenovic and A. Kis, *Nat Nanotechnol*, 2013, **8**, 497-501.